Science
AAAS

Supplementary Materials for

Cilia function as calcium-mediated mechanosensors that instruct left-right asymmetry

Lydia Djenoune *et al*.

Corresponding author: Shiaulou Yuan, shiaulou.yuan@mgh.harvard.edu

Science **379**, 71 (2023)
DOI: 10.1126/science.abq7317

The PDF file includes:

Other Supplementary Material for this manuscript includes the following:

Materials and Methods

Animal Care

Animal handling and procedures adhere to the National Institutes of Health (NIH) Guide for the Care and Use of Laboratory Animals and were approved by the Massachusetts General Hospital Institutional Animal Care and Use Committee. Zebrafish (*Danio rerio*) adults and zebrafish embryos were raised and maintained according to established protocols (*51*). Wild-type (WT) embryos were collected from TUAB or NHGRI-1 adult crosses (*52*). The *pkd2* mutant embryos (*hi4166*) were collected from crosses between heterozygous adult carriers and genotyped at the end of the experiment by PCR as previously reported (*53*). *pkd2* mutant experiments and analysis were performed blindly of genotype. Embryos were staged by somite numbers and previously established criteria (*54*). Small variations in the developmental timeline of the left-right organizer (LRO) might exist between various WT line backgrounds.

Optical deflection of primary cilia in cultured porcine kidney cells

WT LLC-PK1 cells were obtained from and validated by American Type Culture Collection. Cells were cultured in DMEM:F12 growth medium (Life Technologies) containing 5% fetal bovine serum (Life Technologies) and incubated at 37°C with 5% CO_2. Cells were grown to 70% confluency onto coverglass, coverglass-bottom dishes (Mattek) or Cytodex 3 microcarrier beads (Cytiva), and transfected utilizing Lipofectamine 2000 (Life Technologies) according to the manufacturer's protocol in serum-free OptiMEM medium (Life Technologies). After 8 hours, transfection media was replaced with DMEM:F12 media and the cells were serum-starved for 48 hours to induce cilia formation. On the day of imaging, media was replaced with fresh DMEM:F12 media lacking phenol red and serum. During live imaging, cells were mounted and incubated on an inverted stage fitted with an environmental chamber (OKOlab) that maintained conditions at 37°C throughout the experiment or at room temperature. For differential interference contrast (DIC) videomicroscopy studies, cells were imaged on one of two microscopes: (1) an inverted Nikon Eclipse TiE microscope equipped with an add-on home-built optical tweezer unit consisting of a 1064 nm laser (YLR-10-1064-LP, IPG) and a piezo mirror (TT2.10, Piezoconcept) and coupled to the epi-port of the microscope. Trapping was done using a 60x/1.2 water immersion objective (CFI Plan Apo, Nikon). (2) A custom optical tweezers was built around a 135TV Axiovert microscope (Zeiss) as previously described (*55*). Briefly, a 1.5 W diode pumped 1064 nm laser (Smart Laser Systems) was used for trapping. At the sample plane, the trap was controlled in 3D using two piezo mirrors (S-226.00, Physik Instrumente) and a movable lens. The sample was mounted on a coarse positioning stage which was mounted on a nano-positioning stage (P-733.3DD, Physik Instrumente). Trapping was done with either a 100x/1.3 oil immersion (Plan-Neofluar, Zeiss) or a 63x/1.2 water immersion objective (C-Apochromat, Zeiss). For fluorescent cilia studies, cells were transfected with a pCSDest plasmid containing *arl13b:EGFP* (*56*) and imaged on the above Zeiss microscope with an epi-fluorescence LED lamp (Lumencor) or a Nikon spinning disk confocal microscope (Yokogawa W1) with a 488 nm excitation laser. Oscillatory bending of renal primary cilia was applied at a displacement frequency between 0.5 to 2.0 Hz. Cilia were kept in the optical trap and bent for as long as possible, before moving to the next one.

CiliaSPOT: Ciliary Selective Plane Illumination Microscope with Optical Tweezers

The hybrid instrument (**Fig. S3**) combined light sheet microscopy and optical tweezers to enable simultaneous high-speed two-color fluorescence imaging and optomechanical manipulation of LRO cilia in zebrafish embryos. For light sheet fluorescence imaging, a 488 nm diode laser (OBIS,

Coherent) and a diode pumped 561 nm laser (06-DPL 561, Hubner-photonics) were used for excitation. Both lasers were mounted and combined in a laser combiner (C-Flex, Hubner-photonics). Next, the combined beam was expanded to a final diameter of 7.5 mm using a Keplerian telescope (Thorlabs). Then, a graduated iris diaphragm (Thorlabs) was used to adjust the beam diameter depending on the desired light sheet thickness (*32, 57*). To form two excitation arms, the beam was split using a 50/50 non-polarizing beam splitter (Thorlabs). In each excitation arm, a light sheet was generated by a cylindrical lens (Achromat, Thorlabs). The light sheet was then coupled to the illumination objective (10x/0.2 LSM objective, Zeiss) and projected into the sample. To reduce stripping effects, a resonant mirror (SC- 30-10x10-20-1000, EOPS) was placed at the front focal plane of the cylindrical lens to pivot the sheet around the optical axis (*32*). The position of the light sheet in the sample plane was controlled by a kinematic tip/tilt mirror (Thorlabs) placed in a conjugate plane with the back focal plane of the illumination objective. Embryos were embedded in a 1% low-melting point agarose column (Lonza) in a glass capillary (Drummond). The capillary was mounted on a 4D stage made of three orthogonal linear stages (12 mm travel range, M-111.1DG1, PI) and a rotation stage (DDR25/M, Thorlabs). The sample was immersed in a custom machined aluminum chamber (total volume ~ 8 ml) filled with E3 media. For coarse positioning, the sample was imaged with a USB microscope camera with LED lights (Plugable Technologies) mounted opposite to the detection objective. The sample was imaged by a water immersion detection objective (60x/1.1 LUMFLN60XW, WD = 1.5 mm, Olympus) orthogonal to the light sheet. Images were spectrally separated to GCaMP6s (green) and mApple (red) channels using a dichroic (T570lpxr, Chroma) and two emission filters (ET 525/50, ET 630/75, Chroma). The images were projected onto a pair of high sensitivity sCMOS cameras (Prime 95B, 95% QE, Photometrics) using a tube lens (f = 180 mm, Olympus). Image acquisition was controlled by µManager (*58*) and Thorlabs software. For optomechanical manipulation of cilia, a near infrared 1064 nm laser (YLR-10-1064-LP, IPG) was used to form an optical trap. The laser had a minimal operational intensity of 1 W and was adjusted to lower levels using an intensity control unit made of a rotatable half wave plate (CVI laser optics), a polarizing beam splitter and a beam dump (Thorlabs) (*59*). Next, the trapping laser was split using a second polarizing beam splitter (Thorlabs) to create dual independent traps. For each trap, the lateral position at the sample plane was controlled with a two-axis piezo tilt mirror (Nano-MTA2X10, MadCity Labs) placed in a conjugate plane with the back focal plane of the objective (*59, 60*). Axial position of the trap was adjusted by a telescope with a moving lens (Thorlabs) (*59, 60*). For this work, only one of the traps was used. The trapping beam diameter was adjusted by a telescope (Thorlabs) to a final diameter of 6.3 mm to achieve a filling ratio of ~1 (filling ratio = trap beam diameter / imaging objective diameter) (*61*). The trapping laser was coupled to the detection objective using a dichroic mirror (ZT1064rdc, Chroma). The detection objective focused the trapping laser into a diffraction limited spot thus forming the optical trap. Back scattered trapping laser light was filtered out using a short pass filter (ET750sp-2p8, Chroma). The optical trap position was dynamically controlled with a custom LabView (National Instruments) routine (amplitude, frequency and angle of bending). All other optics and optomechanics used including lenses, mirrors, holders, rails and cage systems were purchased from Thorlabs unless mentioned otherwise. The entire instrument was built on a vibration isolation optical table (TMC). Throughout this study, we used 100 mW trap power at the sample plane as it was sufficient to trap LRO cilia. Note that our approach is well beneath the trapping power used in the literature for zebrafish optical tweezer studies, which reported up to 600 mW of trapping power without any negative reported side effects (*62-64*). In **Fig. 1A**, the excitation laser (blue line) is shaped into a light sheet by the cylindrical lens (CL) then is projected onto the sample by the illumination objective (IO). A resonant mirror (RM) pivots the light sheet around the optical axis (z direction) to reduce striping artifacts. The fluorescence signal (orange

line) is collected by the detection objective (DO) and projected onto two cameras (CAM) using a tube lens (TL) and a dichroic mirror (DM). Optical trapping laser (OT, red line) is coupled to the objective by a second dichroic mirror then is focused into the sample plane. A programmable piezo mirror (PM) controls the lateral position of the trap in the sample plane. The sample is mounted in a glass capillary (C) that can be positioned in 4D (x,y,z and rotation).

Estimation of bending forces on LRO cilia by CiliaSPOT

A shape analysis approach was used to estimate the forces exerted by the CiliaSPOT optical tweezers to bend LRO cilia. The cilium was approximated by an elastic micro-rod with a fixed end in a low Reynolds number environment (i.e., inertia is negligible) (*65*). Exerting a force on the free end of the cilium perpendicular to the long axis will cause the cilium to bend (**Fig. S5**). The exerted force can then be calculated as previously described (*65*):

$$F = 3EI\ \frac{d}{L^3}$$

Where F is the optical bending force, EI is the flexural rigidity of the cilium, d is the deflection distance, and L is the length of the cilium. Both L and d are measured from the acquired images. Randomly selected immotile LRO cilia from *c21orf59* knockdown embryos at 1-4 ss were analyzed. The length, bending amplitude, and bending angle for each cilium were measured from 30 images representing ~4 bending cycles. The flexural rigidity was set to 36×10^{-24} N.m^2, measured as previously described (*34*). The calculated bending force was 0.6 ± 0.4 pN (mean ± S.D., n = 73 immotile LRO cilia from 25 *c21orf59* knockdown embryos), in line with previous results (*34*, *35*).

Estimation of in vivo fluid flow forces on LRO cilia

To estimate the in vivo forces exerted by fluid flow to bend LRO cilia, we used the same equation above with d as the average cilium tip displacement (0.7 µm, measured from fast DIC imaging of LRO cilia from wildtype embryos, **Fig. S2** and **Movie S3**), and L as the length of the cilium (7.3 µm, measured average LRO cilia length from *c21orf59* knockdown embryos). The calculated in vivo flow force was 0.1 pN, which was within the same order of magnitude as the estimated CiliaSPOT bending force of 0.6 pN described above. Thus, the applied trap forces were in line with the in vivo flow forces that a cilium is exposed to in the LRO.

CiliaNet: Ciliary Neural Network image-analysis platform

CiliaNet is based on the neural network architecture previously described for automated cardiac functional analysis in zebrafish embryos (*66*). The network was trained to detect LRO cilia from background for each channel of the raw CiliaSPOT datasets. Training datasets were generated from 30 cilia and created via manual segmentation of each cilium in a total of 21,571 images using Fiji (*67*). Image brightness was not normalized prior to training. CiliaNet uses the underlying architecture of SegNet (*66*), with an encoder depth of 4 and an input image matrix of 50x50 pixels to reduce the time required for training. Using the SegNet architecture, images of moving LRO cilia were deconstructed by the encoder to extract local features at varying resolutions, which were then upsampled by the decoder to map each feature weight back to their correct positions relative to the input image. The final decoder layer data was then fed to a multi-class Softmax classifier, which assigns each pixel to their respective label of cilium (white mask) or background (black). Validation of CiliaNet image segmentation accuracy is described in **Fig. S6**. CiliaNet was designed

to process raw datasets of 1200x1200 pixel resolution composed of two channels (GCaMP6s and mApple) and to apply the same segmentation on top of both channels, allowing our ratiometric approach. For each recording, a region of interest, defined by a square box of varying size which depends on the cilium of interest, is apposed on top of the optically bent cilium and segmentation is performed only on this region. For each analyzed cilium, CiliaNet outputs are the following: the segmented annotation of the moving cilium (mask), the extracted mean pixel value of the regions of interest annotated by CiliaNet for GCaMP6s signal, and the extracted mean pixel value of the same regions for the mApple signal.

Zebrafish microinjection of calcium indicators and morpholinos

All transcripts and morpholinos (MO) were microinjected at the one-cell stage using standard protocols (*51*). Procedures for injection of cilia-targeted genetically encoded calcium indicators and morpholinos were followed as previously described (*20, 68, 69*). In brief, *arl13b:GCaMP6s* and *arl13b:mApple* in vitro transcribed mRNA were co-injected with sterile water at a dose of 130 pg each. The previously published *c21orf59* MO (*37*) was injected at a dose of 16 ng (the dose that we previously identified as the minimum one to obtain a strong penetrant phenotype with minimal toxicity), and *pkd2* (*53*) at a dose of 5 ng. The Control MO (CMO) used was a standard control oligo, which also served as a control for developmental delay. All morpholinos were obtained from Gene Tools, LLC. Morphants refer to embryos injected with MOs. For analysis of mesendodermal activity in response to LRO cilia optomechanical stimulation, in addition to the *arl13b:GCaMP6s* and *arl13b:mApple* reporters, WT embryos were co-injected with *HA:GCaMP6s* at a dose of 25 pg.

In vivo imaging of ciliary calcium-responses to optical bending in the zebrafish LRO

Imaging of intraciliary calcium dynamics in response to optical bending was performed using CiliaSPOT. Embryos were mounted in a capillary filled with 1% low-melting agarose (Lonza) and imaged in our custom chamber filled with E3 filtered media. Simultaneous two-channel (GCaMP6s and mApple) recordings were captured at an acquisition rate of 7 Hz at 1200x1200 pixel resolution with no binning and an exposure time of 130 ms. For each embryo, a 900 frame-time window was first recorded to determine the sample's activity at rest (OFF). Next, recordings of 3000 frames each were acquired while LRO cilia were optically bent. Optical bending of LRO cilia was performed with a 1 Hz oscillatory displacement frequency in order to mimic in vivo LRO cilia behavior (**Fig. S2D to F**).

Analysis of intraciliary and cytosolic calcium responses in the zebrafish LRO

For analysis of ciliary calcium response to bending, after acquisition, datasets were first cropped to a 350x350 pixel resolution to isolate the LRO. Movies were next registered using the Fiji plugin NanoJ (*70*) to re-align GCaMP6s and mApple signals for optimal ratiometric analysis (**Fig. S4**). Data were then background subtracted. Movies were subsequently analyzed using CiliaNet to generate an intensity over time plot for all bent cilia for both GCaMP6s and mApple signals. For each imaged LRO, we tweezed as many cilia as technically possible. Cilia were randomly selected for tweezing. However, as ciliary tweezing in vivo in the LRO is an immense technical challenge, we were not always successful in manipulating every LRO cilium due to various limitations (orientation, focal plane, tissue depth, signal-to-noise, etc). We kept in our dataset only the embryos for which we were able to tweeze and analyze the responses for at least 4 cilia. Responses were estimated based on the ratiometric trace of the analyzed cilium. For analysis of cytosolic calcium activity in response to optical bending of LRO cilia, 1200x1200 pixel resolution movies were analyzed. Regions of interest surrounding responding cells were manually defined and their

fluorescence over time was extracted in Fiji. ΔF/F and ΔR/R for both ciliary and cytosolic calcium responses were then calculated using MATLAB (Mathworks) as previously described (*71*). In brief, they were calculated as ΔF/F= (F[t]-F0) or ΔR/R= (R[t]-R0), with F0 and R0 being the average fluorescence of the cilium prior to start of the bending. The total number of cilia per embryo, and number of cilia per LRO quadrant analyzed in our study are summarized in **Table S1** and **Table S2**.

Analysis of CiliaSPOT optical tweezers laser power on calcium activity in the zebrafish LRO

To test the potential effect of our CiliaSPOT trap laser power (100 mW of in plane laser power) on aberrant calcium activity, *c21orf59* embryos expressing (*arl13b:GCaMP6s/mApple*) at 1-4 ss were exposed to a stationary optical trap centered in the LRO. Embryos were embedded in 1% agarose then imaged before and after application of the stationary optical trap using CiliaSPOT. For each condition, the embryos were imaged between 3.5 to 5.0 min and the frequencies of cytosolic calcium transients were manually measured. Note that 100 mW in plane trapping power had no significant impact on calcium activity ($p = 0.25$, paired t-test, $n = 11$ embryos, **Fig. S9**). Further, prior studies have demonstrated that the heat-induced by 100 mW of in plane trapping power is negligible and safe for biophysical studies (*72*).

Optical thermometer temperature calibration

We utilized the temperature sensitive fluorescent dye, Rhodamine B, as an optical thermometer. Rhodamine B (Sigma) was dissolved in ultrapure water (18.2 MΩ.cm resistivity, Milli-Q, Millipore) to a final concentration of 100 µM. 4 mL of the Rhodamine B solution was added to a 35 mm glass bottom dish (D35-20-1.5H, Cellvis) in a temperature-controlled microscope stage (UNO stage incubator, OKOlab) fitted onto an inverted Zeiss Axiovert 200M microscope. Dishes were incubated for 10 minutes to thermally equilibrate and were covered to reduce evaporation. The stage temperature was then increased to 32°C after which it was allowed to passively cool down to room temperature, while Rhodamine B temperature was concurrently measured using a thermocouple sensor. Widefield epi-fluorescence images of Rhodamine B solution were acquired every 2.5 minutes during heating and cooling cycles using a 20x/0.8 objective (Plan Apo, Zeiss), a Rhodamine filter set (filter set 20, Zeiss), a pE-300ultra epi-fluorescent LED light source (CoolLED), and an sCMOS camera (Prime BSI, Photometrics). Rhodamine B fluorescence signal was measured as a function of temperature and showed a linear dependence with a sensitivity of -0.0200 ± 0.0005 (mean ± S.D., $n = 6$ replicates, **Fig. S10A**).

Optical thermometer measurements of temperature changes in CiliaSPOT

Optical thermometer probe was prepared by dissolving 100 µM Rhodamine B in 1% low melt agarose and MQ water. The probe was submerged into the imaging chamber of CiliaSPOT 8 mL of 100 µM Rhodamine B solution (described as above). The probe was imaged for 30 seconds at 10 frames/second. At t = 10 seconds the optical tweezers were allowed to irradiate the sample for 10 seconds. This led to a change in Rhodamine B signal which was converted to temperature change based on the Rhodamine B temperature calibration described above. This experiment was repeated three times at different laser powers (**Fig. S10B**). The temperature increased linearly with the trap laser power at a rate of 9.7 ± 0.5°C/W, in line with prior reports (*72, 73*).

Physical thermometer measurements of temperature changes in CiliaSPOT

We inserted the needle probe of a self-calibrated thermometer with a digital readout near the trapping plane inside the specimen chamber of CiliaSPOT filled with MQ water. The measurement was repeated three times and each recording lasted for a 6-minute total duration, which

corresponds to the duration of our CiliaSPOT LRO cilia deflection recordings. We found the heat elevation by our 100 mW optical tweezers laser to be at 0.1ºC, which was within the margin of error of the thermometer used (± 0.1º C).

Brightfield microscopy, DIC microscopy, and optical trapping of zebrafish LRO cilia

For brightfield or DIC videomicroscopy studies of zebrafish LRO cilia, embryos were imaged on one of two microscopes. The first was an optical trap built as an add-on module to an upright commercial confocal microscope (Zeiss LSM 780). Infrared laser light (laser: JDSU S27-7602-340, 980 nm, 300 mW maximum; controller: Thorlabs CLD1015) was directed into the microscope through the top camera mount. The laser beam was adjusted to have diameter of ~ 4.1 mm, passed through a 200-mm lens (Thorlabs AC254-200-B) to come into focused at the nominal image plane of the camera port, and went on to pass through the built-in tube lens of the microscope and the microscope objective (40X/1.1 Apochromat, water immersion, Zeiss), to form an optical trap of diameter ~ 1.3 microns at the sample. A short-pass dichroic beamsplitter (Semrock FF749-SDi01-25x36x3.0) was used to reflect the laser beam into the camera port, thus allowing the visible light collected by the objective to be routed onto an imaging camera (Zeiss AxioCam MRm). The optical trap was operated simultaneously with the wide-field mode of the microscope, in either bright-field or fluorescence, and observed with the camera. The second was an inverted Zeiss Axiovert 200M microscope equipped with an add-on home-built optical tweezer unit consisting of a 1064nm laser (YLR-10-1064-LP, IPG) and a piezo mirror (TT2.10, Piezoconcept) coupled to the epi-port of the microscope. Trapping was done with a 63x/1.2 water immersion objective (C-Apochromat, Zeiss), a motorized XY stage (AMS2000, ASI), a sCMOS scientific camera (Prime BSI, Photometrics). The setup was controlled by a combination of µManager (*58*) and LabVIEW software (National Instruments).

dand5 in situ hybridization

Whole mount in situ hybridization was performed as previously described (*20*). Briefly, zebrafish embryos were fixed in 4 % paraformaldehyde (in PBS- Tween 0.1 %) overnight at 4°C. The *dand5* probe (gifted from H. Hashimoto, Nagoya University; also referred to as *charon*) was digoxigenin-UTP-labeled and synthesized in vitro (*47*). The hybridized probe was localized using an alkaline phosphatase-coupled anti-digoxigenin antibody (Roche). BM Purple AP substrate (Roche) was used as the chromogenic substrate to produce purple/blue precipitates. Stained embryos were mounted in 1 % low-melting point agarose (Lonza) and images were taken on an upright Leica DM6B microscope with a color camera.

Functional analysis of ciliary mechanosensation in *c21orf59* and *pkd2* knockdown embryos

Embryos were dechorionated using 5 mg/mL pronase (Roche) for 5 minutes and then thoroughly washed 5 times with E3 embryo medium. Embryos were submerged in 1 % low melting point agarose (Lonza) and mounted into a coverglass-bottom petri dish (Mattek or Cellvis) covered by a cover glass with the tailbud mounted towards the imaging objective. Immotile LRO cilia in *c21orf59* and *pkd2* morphant embryos were visualized by brightfield or DIC illumination starting at the 1-somite stage until the 4-somite stage (~1 hour at 28.5°C), which is the critical window for asymmetric intraciliary calcium signaling in the zebrafish LRO (*20*). Each cilium was maintained in the optical trap and bent in an oscillatory fashion at 1 Hz (to mimic in vivo LRO cilia dynamics, **Fig. S2**) for a total of 1 hour in duration. For each embryo, a single LRO cilium was selected and optically bent based on the following criteria: (1) placement on the middle of the dorsal-ventral plane, (2) clear localization to either the left or right side of the LRO, and (3) complete lack of ciliary motility throughout the experiment. For each cilium tweezed, DIC videomicroscopy

recordings were acquired to document the position and deflection. After cilia trapping, embryos were excised from the agarose, raised normally in E3 embryo medium at 28.5°C and either fixed at 8-10 ss for *dand5* expression scoring (when asymmetric expression of *dand5* is robust (*46*)), or scored at 1 dpf for cardiac laterality (as illustrated in **Fig. S11** and **Movie S11**).

In vivo cilia dynamics analysis in the LRO of wildtype zebrafish

Images of the zebrafish LRO cilia were acquired using a customized inverted Zeiss Axiovert 200M microscope equipped with a 63x 1.2 NA water immersion objective (Zeiss, Plan C-Apochromat), DIC illumination and an sCMOS camera (Prime BSI, Photometrics). Wildtype embryos were imaged between bud and 2-somite stages. Recordings were performed at ~40 Hz for ~12.5 seconds. Analysis of the ciliary displacement angle, and displacement frequency were done using Fiji (*67*). For the displacement frequency analysis, the reported value is the mean out of 4 measurements done every 3.125s.

Zebrafish cardiac laterality analysis

Heart jogging was scored at ~30-32 ss (24-26 hpf) by examining heart jogging position across the left-right axis under a standard dissection microscope (Leica) (**Fig. S11** and **Movie S11**) with brightfield illumination as previously described (*20*).

Statistics

Criteria for statistical significance was defined as $p < 0.05$. Data with a $p > 0.05$ was denoted as not significant (ns). Statistical significance is defined as: * $p < 0.05$, ** $p < 0.01$, *** $p < 0.001$, and **** $p < 0.0001$. All statistical tests used to compare datasets are defined in figure legends. All graphs were prepared, and statistical analyses performed using Prism8 (GraphPad), Origin (OriginLab) and Excel (Microsoft), except for $\Delta F/F$ and $\Delta R/R$ traces that were generated using MATLAB (Mathworks).

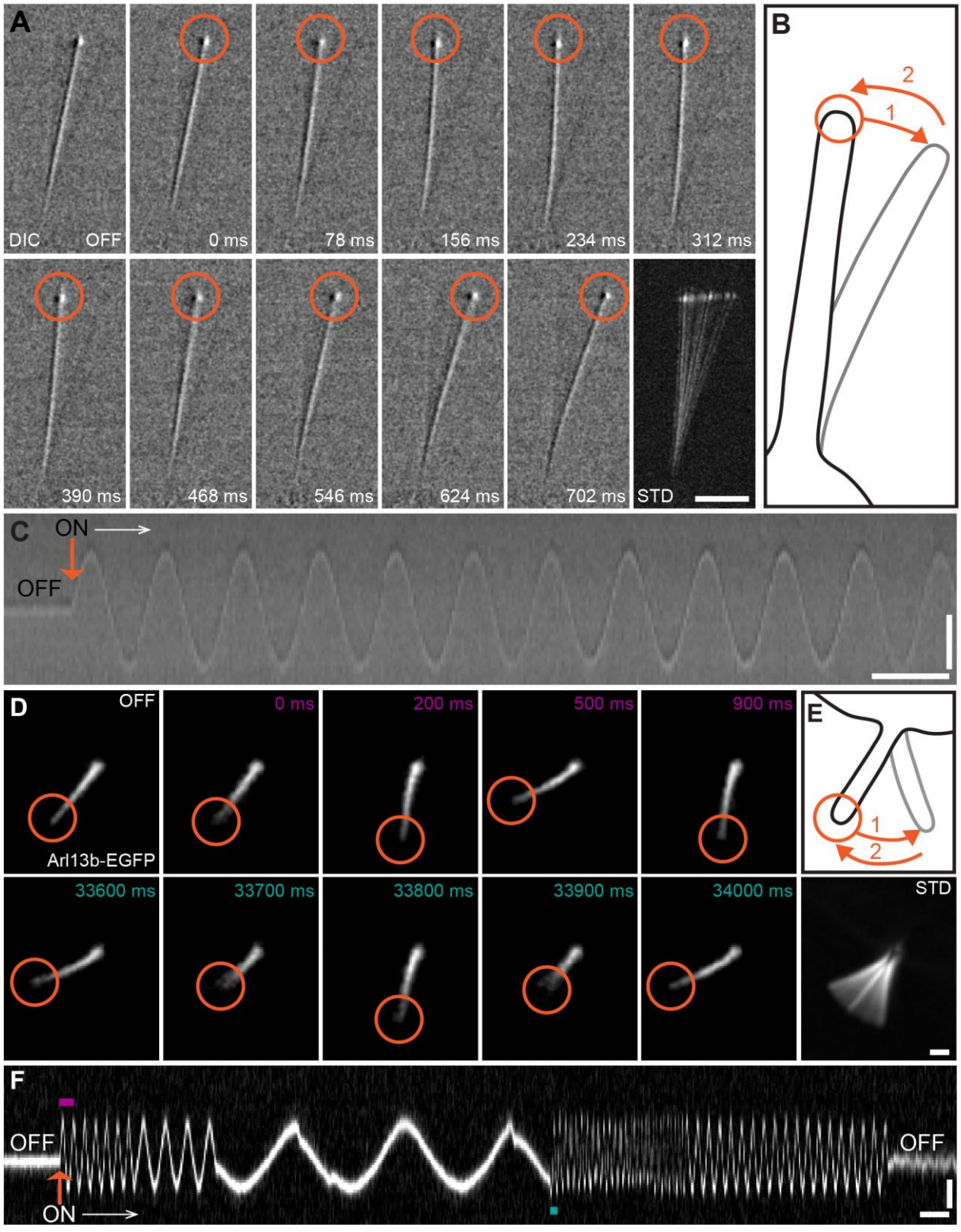

Fig. S1. Optical tweezers enable controlled mechanical manipulation of cilia. (**A-F**) Optical tweezing of pig renal cilia with differential interference contrast (DIC) and fluorescent imaging. (**A**) A single primary cilium from a wildtype LLC-PK1 pig renal cell is visualized by DIC, trapped with optical tweezers and oscillated back and forth by steering the trapping laser with a computer-

controlled piezoelectric-actuated mirror. Scale: 5 µm. (**B**) Illustration of oscillatory motion applied in (A). (**C**) Representative kymograph of the cilium displayed in (A), before (OFF) and during trapping by the optical tweezers (ON, starting at orange arrow). Scales: vertical: 2 µm; horizontal: 1 s. (**D)** A single pig renal primary cilium expressing the fluorescence ciliary marker *arl13b:EGFP* is tweezed and oscillated. Scale: 2 µm. (**E**) Illustration of oscillatory motion applied in (D). (**F**) Representative kymograph of the cilium optically bent in (D) showing its oscillatory motion in response to the different frequencies induced by the optical tweezers (starting at orange arrow, ON, white arrow). Note that the time points highlighted in magenta and in cyan in (D) are associated to the regions of the kymograph highlighted in magenta and cyan respectively. Scales: vertical: 2 µm; horizontal: 2 s. Orange circles indicate where the optical tweezers are targeted. STD represents the standard deviation Z-projection of the montage.

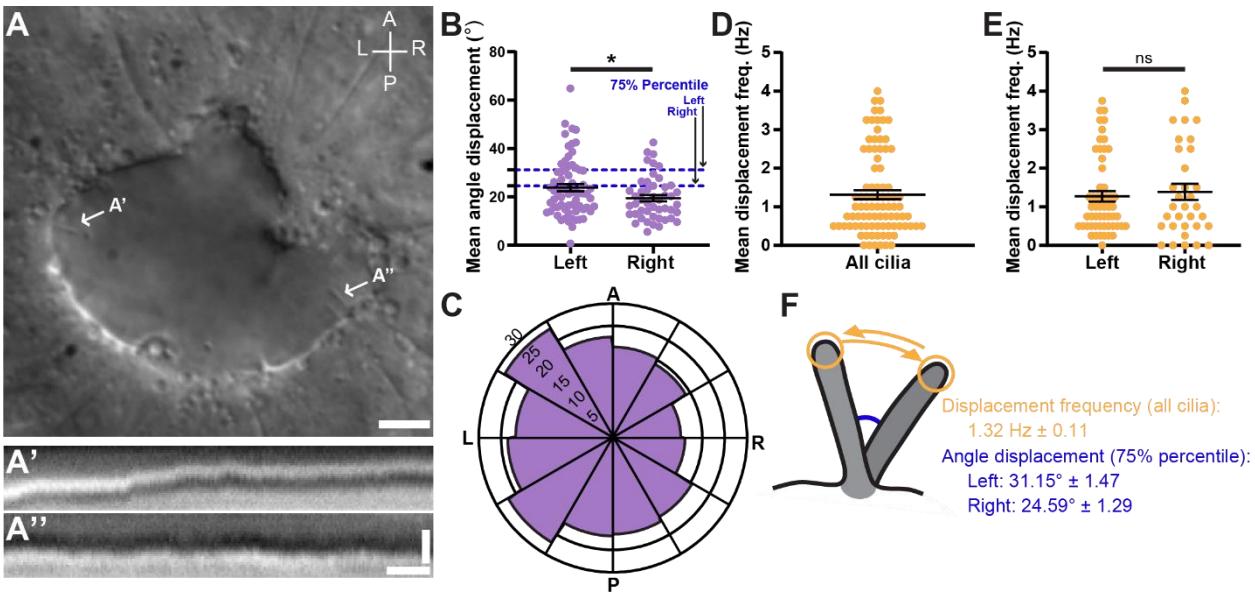

Fig. S2. In vivo imaging of LRO cilia dynamics reveal that left-sided cilia are subject to a higher angle displacement. (**A**) Representative DIC image of the left-right organizer (LRO) of a WT embryo at 1-somite stage. White arrows indicate immotile cilia with kymographs highlighted in A' and A''. Scale: 5 µm. (**A'**) Representative kymograph of a left-sided immotile LRO cilium. (**A''**) Representative kymograph of a right-sided immotile LRO cilium. Scale: vertical: 1 µm, horizontal: 0.5 s. (**B**) Quantification of the mean angle displacement of LRO cilia on the left side (67 cilia from 9 embryos) of the LRO versus the right side (47 cilia from 9 embryos). Mean angle displacement on the left side = 23.83° ± 1.47. Mean angle displacement on the right side = 19.45° ± 1.29. Unpaired two-tailed t-test, * $p < 0.05$ ($p = 0.0361$); Mean ± SEM. (**C**) Spatial mapping of the mean angle displacement of LRO cilia. The rose diagram represents the mean angle displacement of cilia in each depicted region of the LRO. (**D**) Quantification of the mean displacement frequency (freq.) of all LRO cilia analyzed (89 cilia from 9 embryos). Mean displacement frequency of all LRO cilia = 1.32 Hz ± 0.11; Mean ± SEM. (**E**) Quantification of the mean displacement frequency of LRO cilia on the left side (56 cilia from 9 embryos) of the LRO versus the right side (33 cilia from 9 embryos). Mean displacement frequency on the left side = 1.27 Hz ± 0.14. Mean displacement frequency on the right side = 1.39 Hz ± 0.2096. Two-sample t-test, $p = 0.6340$; Mean ± SEM. (**F**) Summary of the quantification of in vivo ciliary dynamics in the LRO. Numbers are the mean ± SEM for the displacement frequency (orange), and the 75% percentiles for each LRO side (blue). A, anterior; P, posterior; L, left; R, right.

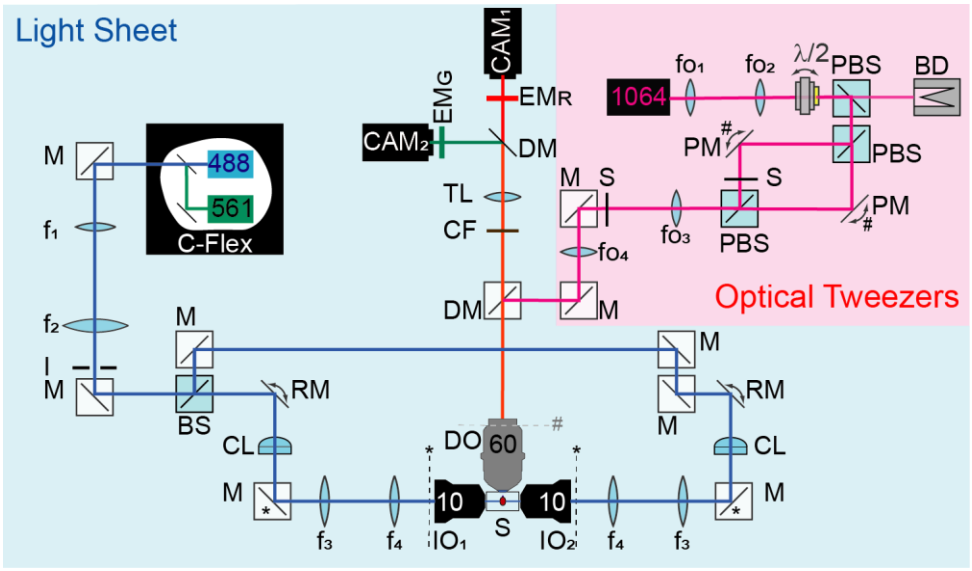

Fig. S3. **CiliaSPOT instrument schematic**. Light sheet: 488: 488 nm excitation laser, 561: 561 nm excitation laser, C-flex: laser combiner, f_1= 19 mm lens, f_2= 200 mm lens, I: graduated iris, BS: 50/50 beam splitter, RM: resonant mirror, CL: 50 mm cylindrical lens, $f_{3\text{-}4}$: 75 mm lens, $IO_{1\text{-}2}$: 10x illumination objective, S: sample, DO: 60x detection objective, CF: clean up filter, TL: tube lens, $EM_{G\text{-}R}$: emission filters, $CAM_{1\text{-}2}$: sCMOS cameras. All lenses used are achromats. Numbers are the lenses focal lengths. * denotes optical conjugate planes. Optical tweezers: 1064: 1064 nm infrared trapping laser, $f_{O1\text{-}2}$: 40 mm lens, λ/2: half wave plate, PBS: polarizing beam splitter, BD: beam dump, PM: piezo mirror, S: shutter, f_{O3}: 150 mm lens, f_{O4}: 200 mm lens, M: mirror, DM: dichroic mirror. All lenses and mirrors are 1064 nm optimized. Numbers are the lenses focal lengths. # denotes optical conjugate planes.

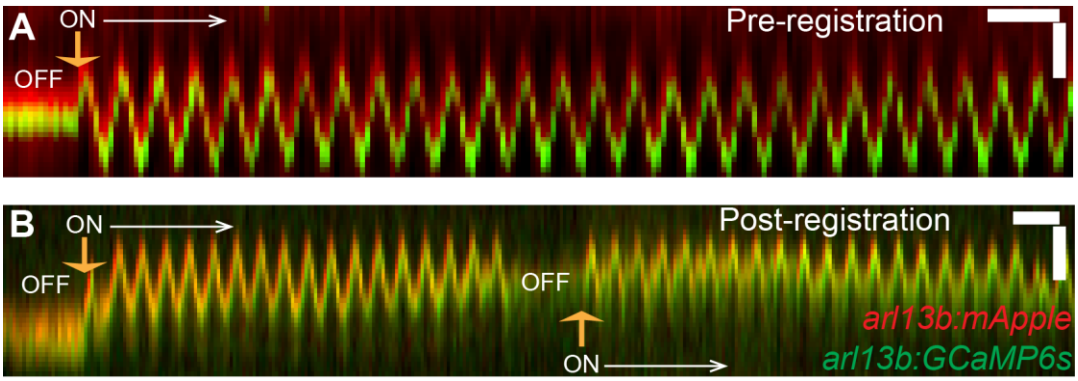

Fig. S4. Tunable bending of LRO cilia by CiliaSPOT and registration for ratiometric intensity analysis. (**A, B**) Representative kymographs of a single LRO cilium from a *c21orf59* knockdown embryo expressing *(arl13b:GCaMP6s/mApple)* being bent by the optical tweezers (starting at orange arrow, ON, white arrow) between 1-4 ss. Note here that in (B), the two signals GCaMP6s and mApple are aligned after registration (see Materials and Methods). Scales: vertical: 2 µm; horizontal: 2 s.

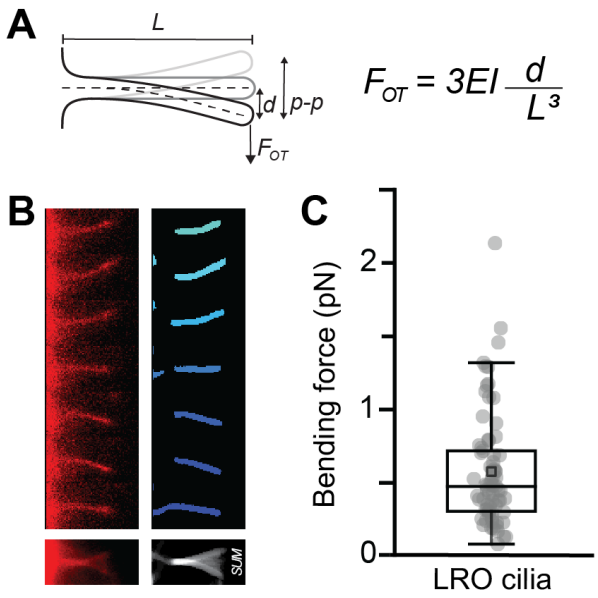

Fig. S5. **Measurement of bending force applied to LRO cilia by CiliaSPOT.** (**A**) An optical force F_{OT} applied on the tip of a cilium of length *L* leading to the bend displacement *d* (half of the peak-to-peak oscillation *p-p*) can be calculated if the flexural rigidity *EI* of the cilium is known. (**B**) Raw and automatically segmented montages of a immotile LRO cilium from *c21orf59* knockdown embryos labeled by *(arl13b:GCaMP6s/mApple)* during one bending cycle with CiliaSPOT between 1-4 ss. Cilium length, bending amplitude and angle can be measured from sum images. (**C**) The average bending force was 0.6 ± 0.4 pN (mean ± S.D., n = 73 immotile LRO cilia from 25 *c21orf59* knockdown embryos).

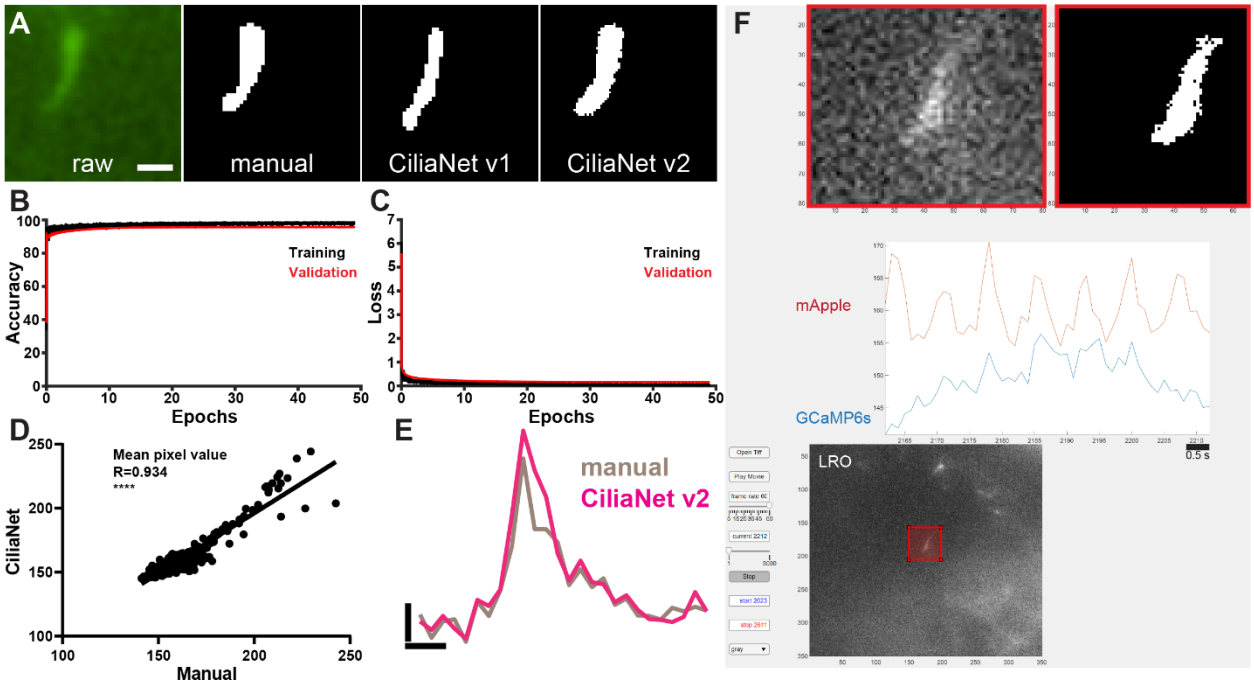

Fig. S6. Training and validation of CiliaNet neural network. (**A**) Representative images of the segmentation generated manually, with CiliaNet version 1 (v1, trained with 1000 manually segmented images), and CiliaNet version 2 (v2, trained with a total of 21571 manually segmented images). (**B**) CiliaNet training and validation accuracy. (**C**) CiliaNet training and validation loss. Each epoch represents 1632 iterations. (**D**) Correlation plot with linear fit of the mean pixel intensity of annotated region between manual and CiliaNet segmentation. **** $p < 0.0001$, Pearson's linear correlation test. R is the linear correlation coefficient. (**E**) Representative intraciliary calcium intensity (ΔF/F) over time plot of a single cilium generated from manual (grey trace) and from CiliaNet segmentation (magenta trace) Scales: vertical: 20% ΔF/F; horizontal: 2 s. (**F**) Representative image of the CiliaNet graphical user interface.

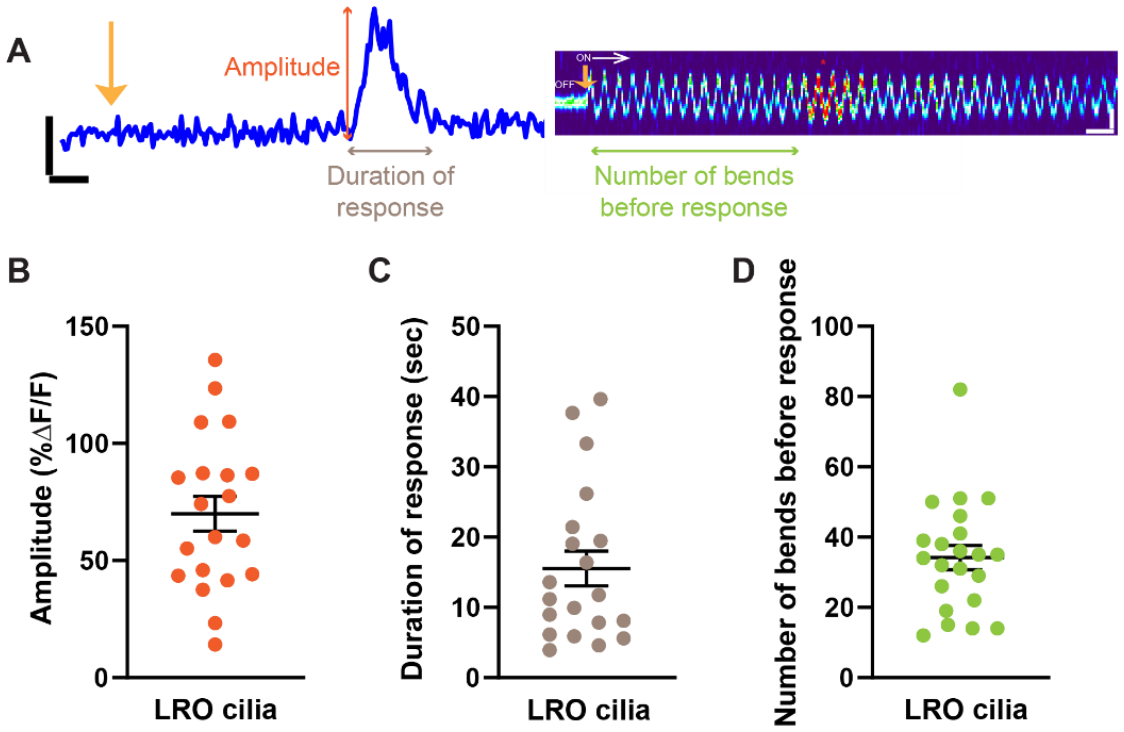

Fig. S7. Features of the LRO ciliary calcium response. (**A**) Representative GCaMP6s intraciliary intensity over time plot of a single immotile LRO cilium from a *c21orf59* knockdown embryo expressing *(arl13b:GCaMP6s/mApple)* between 1-4 ss responding to optical bending annotated with quantified features displayed in (B-D). Optical tweezing starts at orange arrow and white arrow ("ON"). Scales: vertical: 50% ΔF/F; horizontal: 2.5 s. (**B-D**) Ciliary responses to optical bending are characterized by an amplitude of 69.99 ± 7.09 ΔF/F (B), their response lasts on average 15.54 ± 2.36 s (C), and these responses start after the cilium has been bent in an oscillatory manner 34.18 ± 3.45 times (D). Mean ± S.E.M.

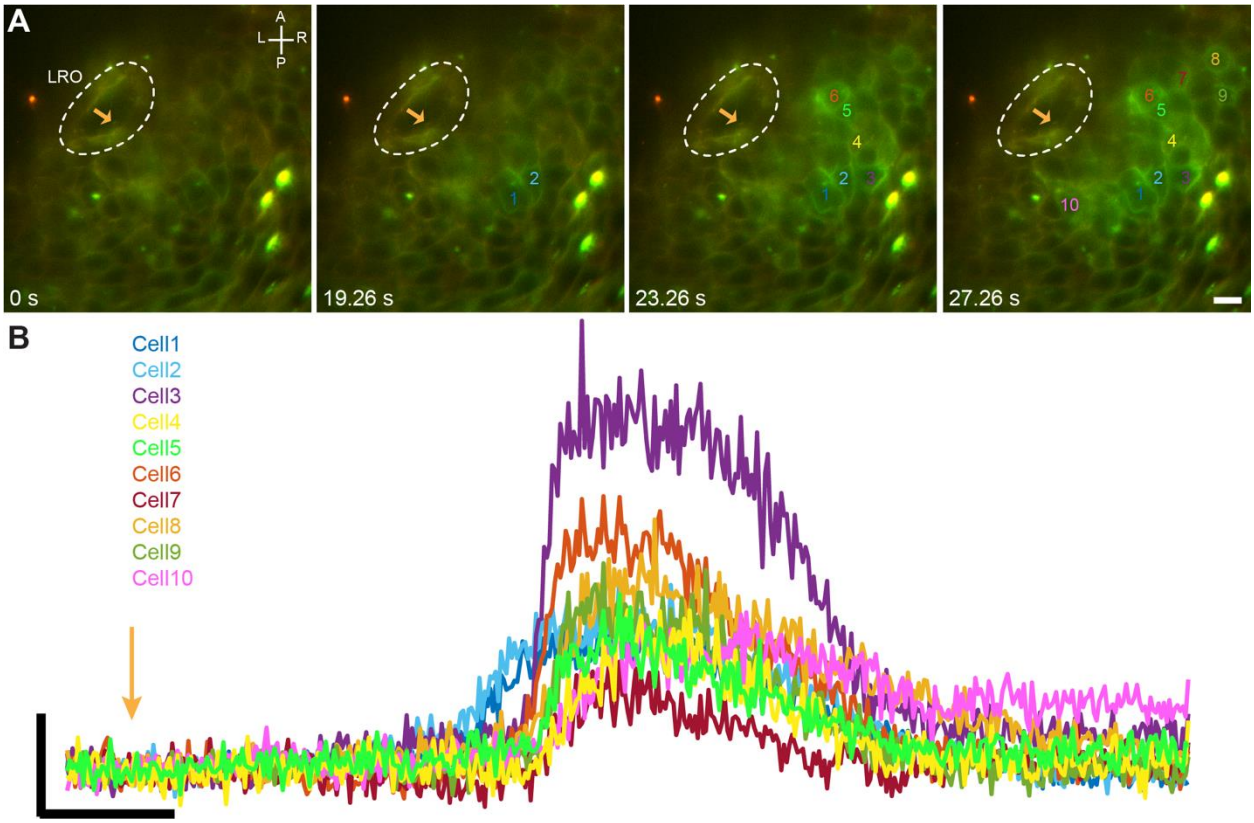

Fig. S8. Optical bending of LRO cilia triggers cytosolic calcium waves in the mesendoderm. (**A**) Representative montage of a cytosolic calcium wave (numbers indicate cells responding by an elevation of calcium) following the optical bending of a single immotile LRO cilium (orange arrow) in a *c21orf59* knockdown embryo expressing *(arl13b:GCaMP6s/mApple)* between 1-4 ss. Numbers indicate time points after start of the bend. LRO is outlined with dashed circle. Scale: 20 µm. (**B**) Ratiometric intensity over time plots of the cytosolic calcium activity in cells highlighted in (A**)**. Each colored trace corresponds to the numbered cells in (A). Scales: vertical: 50% ΔR/R; horizontal: 7 s. A, anterior; P, posterior; L, left; R, right.

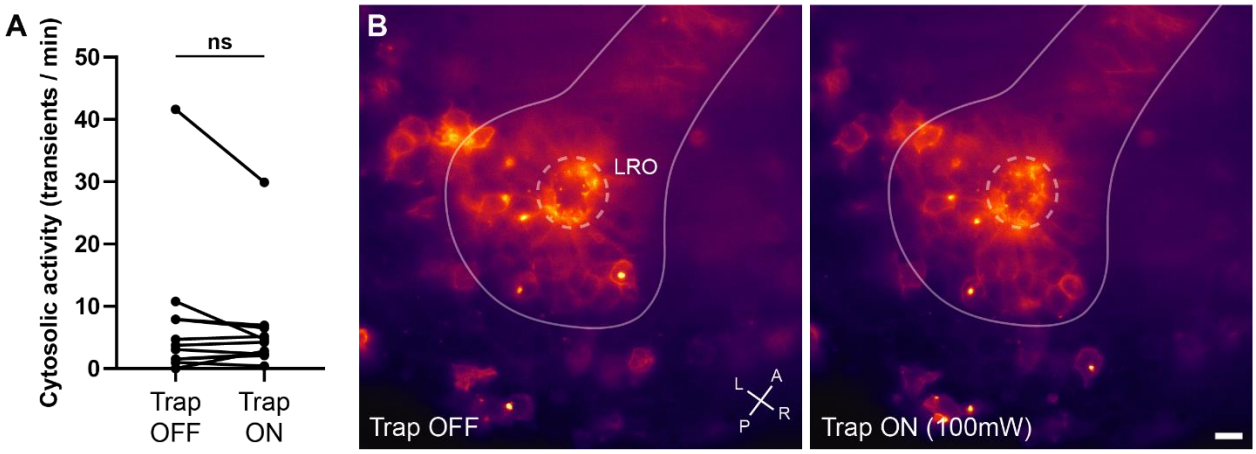

Fig. S9. CiliaSPOT does not induce aberrant calcium activity in the zebrafish LRO. (**A**) Mean frequency of cytosolic activity (number of calcium transients per minute) at rest before (Trap OFF) and after (Trap ON, 100 mW) applying static optical trap to the center of the LRO in *c21orf59* knockdown embryos expressing (*arl13b:GCaMP6s/mApple)* between 1-4 ss. At sample plane, no significant change was observed ($p = 0.25$, paired t-test, $n = 11$ embryos). ns: $p \geq 0.05$. (**B**) Representative fluorescent images of calcium activity in the LRO (dashed circle) when the optical trap is OFF and ON (100 mW). GCaMP6s signal is shown and false-colored with an intensometric scale. Notochord is outlined in solid white line. A, anterior; P, posterior; L, left; R, right. Scale: 20 µm.

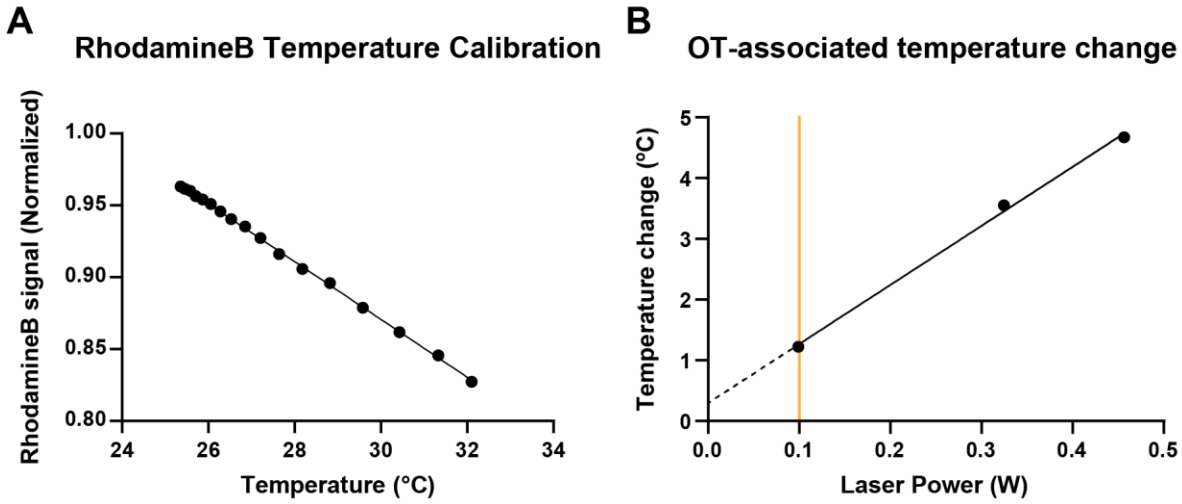

Fig. S10. **Optical thermometer measurements of temperature changes in CiliaSPOT.** (**A**) Representative Rhodamine B temperature sensitivity calibration curve. After reaching 32°C, Rhodamine B solution was allowed to cool down while fluorescent images were acquired at 2.5-minute intervals and their signals were normalized (solid circles) by the maximum signal (prior to heating). From the linear fit (solid line), Rhodamine B sensitivity factor was measured to be -0.02/°C. (**B**) Optical trap (OT) intensity (at the focal plane) in a 100 µM Rhodamine B sample was incrementally increased stepwise and the corresponding temperature changes were measured based on Rhodamine B temperature calibration. The temperature increased linearly with trap intensity at a rate of 9.7°C/W (n = 3 replicates). Orange line represents the 100 mW optical tweezers laser power used in all CiliaSPOT experiments. Dashed line represents y-intercept at 0.2°C, which is factored into our temperature reporting. Error bars are smaller than the symbol size.

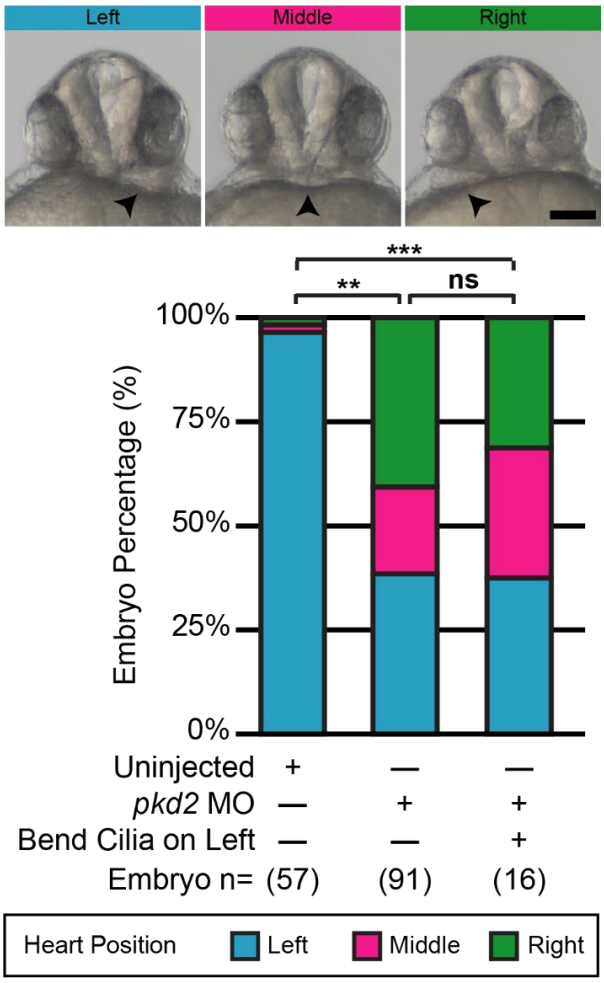

Fig. S11. **LRO ciliary mechanical stimulation is not sufficient to restore proper cardiac laterality in *pkd2* knockdown embryos.** Representative images showing the heart jogging position (black arrowhead) in 1 dpf zebrafish embryos. Embryos are seen from the ventral side, showing normal left (blue) and abnormal middle (magenta) and right-sided (green) heart tubes. The graph represents percentage of uninjected and *pkd2* morphants (MOs) displaying normal left-sided (blue) and abnormal right-sided (green) or middle positioned (magenta) cardiac jogging. For uninjected (n = 57) embryos, 96.5% of embryos displayed normal left-sided heart position. For *pkd2* morphants without cilia deflection (n = 91), 38.5% of embryos had normal left-sided heart jogging, 20.9% had middle positioned hearts and 40.6% had right-sided hearts, indicating a randomized LR defect when compared to uninjected controls ($p = 0.0011$). In *pkd2* morphants with a single cilium deflected on the left-side of the LRO (n = 16), 37.5% of embryos had a left-sided heart, 31.25% showed a middle positioned one, and 31.25% had their heart on the right-side, showing no statistical difference with the *pkd2* embryos that were not optically tweezed ($p = 0.9999$). n = total number of embryos analyzed. Statistical comparison was analyzed by one-way ANOVA with Tukey's multiple comparison test; ** $p < 0.01$, *** $p < 0.001$ and ns: $p \geq 0.05$. Scale: 100 µm.

Condition	Embryo ID	Total number of cilia analyzed per embryo
c21orf59 MO	1	8
c21orf59 MO	2	8
c21orf59 MO	3	15
c21orf59 MO	4	4
c21orf59 MO	5	7
c21orf59 MO	6	6
c21orf59 MO	7	12
c21orf59 MO	8	8
c21orf59 MO	9	4
c21orf59 MO	10	7
c21orf59 MO	11	4
c21orf59 MO	12	5
pkd2 MO	1	9
pkd2 MO	2	5
pkd2 MO	3	9
pkd2 MO	4	4
pkd2 MO	5	4
pkd2 MO	6	7
pkd2 MO	7	8
pkd2 MO	8	4
pkd2 MO	9	8
pkd2 MO	10	8
pkd2 MO	11	9
pkd2 MO	12	8
pkd2 MO	13	6
pkd2 MO	14	10
pkd2 MO	15	7
pkd2 MO	16	8
pkd2 MO	17	5
$pkd2^{+/+}$ sibling	1	5
$pkd2^{+/+}$ sibling	2	9
$pkd2^{+/+}$ sibling	3	6
$pkd2^{+/+}$ sibling	4	12
$pkd2^{+/-}$ sibling	1	8
$pkd2^{+/-}$ sibling	2	14
$pkd2^{+/-}$ sibling	3	8
$pkd2^{+/-}$ sibling	4	18
$pkd2^{+/-}$ sibling	5	4
$pkd2^{+/-}$ sibling	6	17
$pkd2^{+/-}$ sibling	7	6
$pkd2^{+/-}$ sibling	8	6
$pkd2^{+/-}$ sibling	9	10
$pkd2^{+/-}$ sibling	10	4

pkd2$^{-/-}$ mutant	1	8
pkd2$^{-/-}$ mutant	2	7
pkd2$^{-/-}$ mutant	3	5
pkd2$^{-/-}$ mutant	4	13
pkd2$^{-/-}$ mutant	5	5
WT for angle displacement	1	23
WT for angle displacement	2	22
WT for angle displacement	3	5
WT for angle displacement	4	14
WT for angle displacement	5	12
WT for angle displacement	6	11
WT for angle displacement	7	16
WT for angle displacement	8	5
WT for angle displacement	9	7

Table S1. Summary of the number of cilia analyzed per embryo and experimental condition. Detailed breakdown of the number of LRO cilia tweezed or imaged in each condition. MO, morphant

Condition	Quadrant ID				Total
	AL	PL	PR	AR	
c21orf59 MO	36	12	18	22	88
pkd2 MO	39	27	26	27	119
pkd2$^{+/+;\ +/-}$ sibling	31	28	35	33	127
pkd2$^{-/-}$ mutant	10	8	7	13	38
WT for angle displacement	40	27	28	19	115

Table S2. Summary of the number of cilia analyzed per LRO quadrant and experimental condition. Detailed breakdown of the number of LRO cilia tweezed or imaged per quadrant. AL, anterior-left; PL, posterior-left; PR, posterior-right; AR, anterior-right; MO, morphant; WT, wild type.

Movie S1. Optical trapping and bending of primary cilia in LLCPK1 epithelial renal cells. A primary cilium (~18 µm) was trapped at the tip then bent at a frequency of 1 Hz and amplitude of ~5 µm (peak to peak). Raw images were background subtracted and 1pixel Gaussian smoothed. The bright spot at the tip of the cilium is a trapped debris present in the culture medium. Data recorded at 25 Hz, displayed here at 25 frames per second (fps). Scale: 5 µm.

Movie S2. Optical trapping and bending of Arl13b:EGFP positive cilia in LLCPK1 epithelial renal cells. A cilium was trapped at the tip then bent at different frequencies to demonstrate the versatility and full control of our system. Data recorded at 10 Hz, displayed here at 30 fps. Trap OFF and ON denote the state of the optical tweezers. Scale: 10 µm.

Movie S3. In vivo ciliary dynamics in the zebrafish LRO at the 1-somite stage. Representative movie of in vivo cilia dynamics in a wild-type LRO at the 1 somite stage via high-resolution DIC microscopy. White boxes (A' and A") highlight the two immotile LRO cilia magnified in the upper part of the movie, and the two cilia displayed in **Fig. S2**. A, anterior; P, posterior; L, left; R, right. Scales: 10 µm; inset (A''): 2 µm. Data recorded at 40 Hz, displayed here at 40 fps.

Movie S4. Optical bending of cilia in the zebrafish LRO. Representative movie of a GCaMP6s positive immotile LRO cilium from a *c21orf59* knockdown embryo expressing (*arl13b:GCaMP6s/mApple)* at the 1-4 somite stage being trapped and bent at a frequency of 1 Hz. Data recorded at 7 Hz, displayed here at 15 fps. Scale: 2 µm. OFF and ON denote the state of the optical tweezers. Time indicates the oscillatory bending induced by the optical tweezers.

Movie S5. Tracking and segmentation of optically bent LRO cilia by CiliaNet. Representative movies of the segmentation generated manually, with CiliaNet version 1, and CiliaNet version 2 compared to the movie of the optically bent cilium (raw). Data recorded at 7 Hz, displayed here at 15 fps. Scale: 2 µm.

Movie S6. LRO ciliary calcium transient in response to oscillatory optical bending. Representative movie of a intraciliary calcium transient observed in a immotile LRO cilium from a *c21orf59* knockdown embryo expressing (*arl13b:GCaMP6s/mApple)* at the 1-4 somite stage after oscillatory optical bending generated at 1 Hz. Ratiometric signal is displayed here. Data recorded at 7 Hz, displayed here at 15 fps. Scale: 2 µm. Time indicates the oscillatory bending induced by the optical tweezers.

Movie S7. Intraciliary calcium oscillations in response to oscillatory optical bending in LRO. Representative movie of intraciliary calcium oscillations observed in a immotile LRO cilium from a *c21orf59* knockdown embryo expressing (*arl13b:GCaMP6s/mApple)* at the 1-4 somite stage after oscillatory optical bending generated at 1 Hz. Ratiometric signal is displayed here. Data recorded at 7 Hz, displayed here at 15 fps. Scale: 2 µm. Time indicates the oscillatory bending induced by the optical tweezers.

Movie S8. Mesendodermal cytosolic calcium responses after LRO cilia optical bending. Representative movie of cytosolic calcium activity in the cells of the mesendoderm after optical bending of a immotile LRO cilium from a *c21orf59* knockdown embryo expressing (*arl13b:GCaMP6s;arl13b:mApple;HA:GCaMP6s)* at the 1-4 somite stage. GCaMP6s (green) and mApple (red) signals are displayed here. Data recorded at 7 Hz, displayed here at 100 fps. Scale:

10 µm. White arrow indicates the LRO cilium optically bent by CiliaSPOT in an oscillatory motion. OFF and ON indicate when the oscillatory bending was induced by the optical tweezers.

Movie S9. CiliaSPOT does not induce aberrant calcium activity in the zebrafish LRO. Representative movie of calcium activity when static optical trap is applied at 100 mW to the LRO a *c21orf59* knockdown embryo expressing (*arl13b:GCaMP6s/mApple)* at the 1-4 somite stage. The movie shows the calcium activity before (Trap OFF) and after a stationary optical trap is applied at the center of the LRO (Trap ON). Data recorded at 7 Hz and averaged to 1 Hz, displayed here at 60 fps. GCaMP6s signal is shown and false-colored with an intensometric scale.

Movie S10. Absence of intraciliary calcium transients in optically deflected LRO cilia in *pkd2* knockdown embryos. Representative movie of the absence of intraciliary calcium transients in a immotile LRO cilium from a *pkd2* knockdown embryo expressing (*arl13b:GCaMP6s/mApple)* at the 1-4 somite stage while being optically tweezed. Data recorded at 7 Hz, displayed here at 15 fps. Scale: 2 µm. Time indicates the oscillatory bending induced by the optical tweezers.

Movie S11. Analysis of cardiac laterality in zebrafish embryos. Representative movies showing the heart position (cardiac jogging) in zebrafish embryos at 1 day post fertilization. Embryos are seen from the ventral side, with normal (left) and abnormal middle and right heart loops. Movies recorded and played in real time. Scale: 10 µm.

1. J. McGrath, S. Somlo, S. Makova, X. Tian, M. Brueckner, Two populations of node monocilia initiate left-right asymmetry in the mouse. *Cell* **114**, 61–73 (2003). doi:10.1016/S0092-8674(03)00511-7 Medline

2. Y. Okada, S. Nonaka, Y. Tanaka, Y. Saijoh, H. Hamada, N. Hirokawa, Abnormal nodal flow precedes situs inversus in iv and inv mice. *Mol. Cell* **4**, 459–468 (1999). doi:10.1016/S1097-2765(00)80197-5 Medline

3. S. Nonaka, H. Shiratori, Y. Saijoh, H. Hamada, Determination of left-right patterning of the mouse embryo by artificial nodal flow. *Nature* **418**, 96–99 (2002). doi:10.1038/nature00849 Medline

4. S. Nonaka, Y. Tanaka, Y. Okada, S. Takeda, A. Harada, Y. Kanai, M. Kido, N. Hirokawa, Randomization of left-right asymmetry due to loss of nodal cilia generating leftward flow of extraembryonic fluid in mice lacking KIF3B motor protein. *Cell* **95**, 829–837 (1998). doi:10.1016/S0092-8674(00)81705-5 Medline

5. S. Yoshiba, H. Shiratori, I. Y. Kuo, A. Kawasumi, K. Shinohara, S. Nonaka, Y. Asai, G. Sasaki, J. A. Belo, H. Sasaki, J. Nakai, B. Dworniczak, B. E. Ehrlich, P. Pennekamp, H. Hamada, Cilia at the node of mouse embryos sense fluid flow for left-right determination via Pkd2. *Science* **338**, 226–231 (2012). doi:10.1126/science.1222538 Medline

6. M. Levin, R. L. Johnson, C. D. Stern, M. Kuehn, C. Tabin, A molecular pathway determining left-right asymmetry in chick embryogenesis. *Cell* **82**, 803–814 (1995). doi:10.1016/0092-8674(95)90477-8 Medline

7. A. Schweickert, P. Vick, M. Getwan, T. Weber, I. Schneider, M. Eberhardt, T. Beyer, A. Pachur, M. Blum, The nodal inhibitor Coco is a critical target of leftward flow in Xenopus. *Curr. Biol.* **20**, 738–743 (2010). doi:10.1016/j.cub.2010.02.061 Medline

8. J. J. Essner, J. D. Amack, M. K. Nyholm, E. B. Harris, H. J. Yost, Kupffer's vesicle is a ciliated organ of asymmetry in the zebrafish embryo that initiates left-right development of the brain, heart and gut. *Development* **132**, 1247–1260 (2005). doi:10.1242/dev.01663 Medline

9. P. Sampaio, R. R. Ferreira, A. Guerrero, P. Pintado, B. Tavares, J. Amaro, A. A. Smith, T. Montenegro-Johnson, D. J. Smith, S. S. Lopes, Left-right organizer flow dynamics: How much cilia activity reliably yields laterality? *Dev. Cell* **29**, 716–728 (2014). doi:10.1016/j.devcel.2014.04.030 Medline

10. N. Okabe, B. Xu, R. D. Burdine, Fluid dynamics in zebrafish Kupffer's vesicle. *Dev. Dyn.* **237**, 3602–3612 (2008). doi:10.1002/dvdy.21730 Medline

11. J. J. Essner, K. J. Vogan, M. K. Wagner, C. J. Tabin, H. J. Yost, M. Brueckner, Conserved function for embryonic nodal cilia. *Nature* **418**, 37–38 (2002). doi:10.1038/418037a Medline

12. A. G. Kramer-Zucker, F. Olale, C. J. Haycraft, B. K. Yoder, A. F. Schier, I. A. Drummond, Cilia-driven fluid flow in the zebrafish pronephros, brain and Kupffer's vesicle is required for normal organogenesis. *Development* **132**, 1907–1921 (2005). doi:10.1242/dev.01772 Medline

13. W. Supatto, S. E. Fraser, J. Vermot, An all-optical approach for probing microscopic flows in living embryos. *Biophys. J.* **95**, L29–L31 (2008). doi:10.1529/biophysj.108.137786 Medline

14. L. Djenoune, K. Berg, M. Brueckner, S. Yuan, A change of heart: New roles for cilia in cardiac development and disease. *Nat. Rev. Cardiol.* **19**, 211–227 (2022). doi:10.1038/s41569-021-00635-z Medline

15. R. B. Little, D. P. Norris, Right, left and cilia: How asymmetry is established. *Semin. Cell Dev. Biol.* **110**, 11–18 (2021). doi:10.1016/j.semcdb.2020.06.003 Medline

16. R. R. Ferreira, A. Vilfan, F. Jülicher, W. Supatto, J. Vermot, Physical limits of flow sensing in the left-right organizer. *eLife* **6**, e25078 (2017). doi:10.7554/eLife.25078 Medline

17. R. R. Ferreira, H. Fukui, R. Chow, A. Vilfan, J. Vermot, The cilium as a force sensor-myth versus reality. *J. Cell Sci.* **132**, jcs213496 (2019). doi:10.1242/jcs.213496

18. Y. Tanaka, Y. Okada, N. Hirokawa, FGF-induced vesicular release of Sonic hedgehog and retinoic acid in leftward nodal flow is critical for left-right determination. *Nature* **435**, 172–177 (2005). doi:10.1038/nature03494 Medline

19. C. J. Tabin, K. J. Vogan, A two-cilia model for vertebrate left-right axis specification. *Genes Dev.* **17**, 1–6 (2003). doi:10.1101/gad.1053803 Medline

20. S. Yuan, L. Zhao, M. Brueckner, Z. Sun, Intraciliary calcium oscillations initiate vertebrate left-right asymmetry. *Curr. Biol.* **25**, 556–567 (2015). doi:10.1016/j.cub.2014.12.051 Medline

21. D. Takao, T. Nemoto, T. Abe, H. Kiyonari, H. Kajiura-Kobayashi, H. Shiratori, S. Nonaka, Asymmetric distribution of dynamic calcium signals in the node of mouse embryo during left-right axis formation. *Dev. Biol.* **376**, 23–30 (2013). doi:10.1016/j.ydbio.2013.01.018 Medline

22. H. A. Praetorius, K. R. Spring, Bending the MDCK cell primary cilium increases intracellular calcium. *J. Membr. Biol.* **184**, 71–79 (2001). doi:10.1007/s00232-001-0075-4 Medline

23. S. M. Nauli, F. J. Alenghat, Y. Luo, E. Williams, P. Vassilev, X. Li, A. E. H. Elia, W. Lu, E. M. Brown, S. J. Quinn, D. E. Ingber, J. Zhou, Polycystins 1 and 2 mediate mechanosensation in the primary cilium of kidney cells. *Nat. Genet.* **33**, 129–137 (2003). doi:10.1038/ng1076 Medline

24. M. Delling, A. A. Indzhykulian, X. Liu, Y. Li, T. Xie, D. P. Corey, D. E. Clapham, Primary cilia are not calcium-responsive mechanosensors. *Nature* **531**, 656–660 (2016). doi:10.1038/nature17426 Medline

25. S. Su, S. C. Phua, R. DeRose, S. Chiba, K. Narita, P. N. Kalugin, T. Katada, K. Kontani, S. Takeda, T. Inoue, Genetically encoded calcium indicator illuminates calcium dynamics in primary cilia. *Nat. Methods* **10**, 1105–1107 (2013). doi:10.1038/nmeth.2647 Medline

26. A. Ashkin, K. Schütze, J. M. Dziedzic, U. Euteneuer, M. Schliwa, Force generation of organelle transport measured in vivo by an infrared laser trap. *Nature* **348**, 346–348 (1990). doi:10.1038/348346a0 Medline

27. A. Ashkin, J. M. Dziedzic, J. E. Bjorkholm, S. Chu, Observation of a single-beam gradient force optical trap for dielectric particles. *Opt. Lett.* **11**, 288 (1986). doi:10.1364/OL.11.000288 Medline

28. K. Svoboda, S. M. Block, Biological applications of optical forces. *Annu. Rev. Biophys. Biomol. Struct.* **23**, 247–285 (1994). doi:10.1146/annurev.bb.23.060194.001335 Medline

29. A. K. O'Connor, E. B. Malarkey, N. F. Berbari, M. J. Croyle, C. J. Haycraft, P. D. Bell, P. Hohenstein, R. A. Kesterson, B. K. Yoder, An inducible CiliaGFP mouse model for in vivo visualization and analysis of cilia in live tissue. *Cilia* **2**, 8 (2013). doi:10.1186/2046-2530-2-8 Medline

30. J. G. Goetz, E. Steed, R. R. Ferreira, S. Roth, C. Ramspacher, F. Boselli, G. Charvin, M. Liebling, C. Wyart, Y. Schwab, J. Vermot, Endothelial cilia mediate low flow sensing during zebrafish vascular development. *Cell Rep.* **6**, 799–808 (2014). doi:10.1016/j.celrep.2014.01.032 Medline

31. B. Tavares, R. Jacinto, P. Sampaio, S. Pestana, A. Pinto, A. Vaz, M. Roxo-Rosa, R. Gardner, T. Lopes, B. Schilling, I. Henry, L. Saúde, S. S. Lopes, Notch/Her12 signalling modulates, motile/immotile cilia ratio downstream of *Foxj1a* in zebrafish left-right organizer. *eLife* **6**, e25165 (2017). doi:10.7554/eLife.25165 Medline

32. J. Huisken, D. Y. Stainier, Even fluorescence excitation by multidirectional selective plane illumination microscopy (mSPIM). *Opt. Lett.* **32**, 2608–2610 (2007). doi:10.1364/OL.32.002608 Medline

33. T. V. Truong, W. Supatto, D. S. Koos, J. M. Choi, S. E. Fraser, Deep and fast live imaging with two-photon scanned light-sheet microscopy. *Nat. Methods* **8**, 757–760 (2011). doi:10.1038/nmeth.1652 Medline

34. C. Battle, C. M. Ott, D. T. Burnette, J. Lippincott-Schwartz, C. F. Schmidt, Intracellular and extracellular forces drive primary cilia movement. *Proc. Natl. Acad. Sci. U.S.A.* **112**, 1410–1415 (2015). doi:10.1073/pnas.1421845112 Medline

35. A. Resnick, Use of optical tweezers to probe epithelial mechanosensation. *J. Biomed. Opt.* **15**, 015005 (2010). doi:10.1117/1.3316378 Medline

36. K. Mizuno, K. Shiozawa, T. A. Katoh, K. Minegishi, T. Ide, Y. Ikawa, H. Nishimura, K. Takaoka, T. Itabashi, A. H. Iwane, J. Nakai, H. Shiratori, H. Hamada, Role of Ca^{2+} transients at the node of the mouse embryo in breaking of left-right symmetry. *Sci. Adv.* **6**, eaba1195 (2020). doi:10.1126/sciadv.aba1195 Medline

37. C. Austin-Tse, J. Halbritter, M. A. Zariwala, R. M. Gilberti, H. Y. Gee, N. Hellman, N. Pathak, Y. Liu, J. R. Panizzi, R. S. Patel-King, D. Tritschler, R. Bower, E. O'Toole, J. D. Porath, T. W. Hurd, M. Chaki, K. A. Diaz, S. Kohl, S. Lovric, D.-Y. Hwang, D. A. Braun, M. Schueler, R. Airik, E. A. Otto, M. W. Leigh, P. G. Noone, J. L. Carson, S. D. Davis, J. E. Pittman, T. W. Ferkol, J. J. Atkinson, K. N. Olivier, S. D. Sagel, S. D. Dell, M. Rosenfeld, C. E. Milla, N. T. Loges, H. Omran, M. E. Porter, S. M. King, M. R. Knowles, I. A. Drummond, F. Hildebrandt, Zebrafish Ciliopathy Screen Plus Human Mutational Analysis Identifies C21orf59 and CCDC65 Defects as Causing Primary Ciliary Dyskinesia. *Am. J. Hum. Genet.* **93**, 672–686 (2013). doi:10.1016/j.ajhg.2013.08.015 Medline

38. M. T. Boskovski, S. Yuan, N. B. Pedersen, C. K. Goth, S. Makova, H. Clausen, M. Brueckner, M. K. Khokha, The heterotaxy gene GALNT11 glycosylates Notch to orchestrate cilia type and laterality. *Nature* **504**, 456–459 (2013). doi:10.1038/nature12723 Medline

39. D. Moreau, C. Lefort, R. Burke, P. Leveque, R. P. O'Connor, Rhodamine B as an optical thermometer in cells focally exposed to infrared laser light or nanosecond pulsed electric fields. *Biomed. Opt. Express* **6**, 4105–4117 (2015). doi:10.1364/BOE.6.004105 Medline

40. P. G. DeCaen, M. Delling, T. N. Vien, D. E. Clapham, Direct recording and molecular identification of the calcium channel of primary cilia. *Nature* **504**, 315–318 (2013). doi:10.1038/nature12832 Medline

41. M. Delling, P. G. DeCaen, J. F. Doerner, S. Febvay, D. E. Clapham, Primary cilia are specialized calcium signalling organelles. *Nature* **504**, 311–314 (2013). doi:10.1038/nature12833 Medline

42. S. J. Kleene, N. K. Kleene, Inward Ca^{2+} current through the polycystin-2-dependent channels of renal primary cilia. *Am. J. Physiol. Renal Physiol.* **320**, F1165–F1173 (2021). doi:10.1152/ajprenal.00062.2021 Medline

43. P. Pennekamp, C. Karcher, A. Fischer, A. Schweickert, B. Skryabin, J. Horst, M. Blum, B. Dworniczak, The ion channel polycystin-2 is required for left-right axis determination in mice. *Curr. Biol.* **12**, 938–943 (2002). doi:10.1016/S0960-9822(02)00869-2 Medline

44. B. W. Bisgrove, B. S. Snarr, A. Emrazian, H. J. Yost, Polaris and Polycystin-2 in dorsal forerunner cells and Kupffer's vesicle are required for specification of the zebrafish left-right axis. *Dev. Biol.* **287**, 274–288 (2005). doi:10.1016/j.ydbio.2005.08.047 Medline

45. J. Schottenfeld, J. Sullivan-Brown, R. D. Burdine, Zebrafish curly up encodes a Pkd2 ortholog that restricts left-side-specific expression of southpaw. *Development* **134**, 1605–1615 (2007). doi:10.1242/dev.02827 Medline

46. S. S. Lopes, R. Lourenço, L. Pacheco, N. Moreno, J. Kreiling, L. Saúde, Notch signalling regulates left-right asymmetry through ciliary length control. *Development* **137**, 3625–3632 (2010). doi:10.1242/dev.054452 Medline

47. H. Hashimoto, M. Rebagliati, N. Ahmad, O. Muraoka, T. Kurokawa, M. Hibi, T. Suzuki, The Cerberus/Dan-family protein Charon is a negative regulator of Nodal signaling during left-right patterning in zebrafish. *Development* **131**, 1741–1753 (2004). doi:10.1242/dev.01070 Medline

48. T. A. Katoh, T. Omori, K. Mizuno, X. Sai, K. Minegishi, Y. Ikawa, H. Nishimura, T. Itabashi, E. Kajikawa, S. Hiver, A. H. Iwane, T. Ishikawa, Y. Okada, T. Nishizaka, H. Hamada, Immotile cilia mechanically sense the direction of fluid flow for left-right determination. *Science.* **379**, 66–71 (2023). doi:10.1126/science.abq8148

49. K. Shinohara, A. Kawasumi, A. Takamatsu, S. Yoshiba, Y. Botilde, N. Motoyama, W. Reith, B. Durand, H. Shiratori, H. Hamada, Two rotating cilia in the node cavity are sufficient to break left-right symmetry in the mouse embryo. *Nat. Commun.* **3**, 622 (2012). doi:10.1038/ncomms1624 Medline

50. L. Djenoune, M. Mahamdeh, T. V. Truong, C. T. Nguyen, S. E. Fraser, M. Brueckner, J. Howard, S. Yuan, CiliaNet: a deep learning tool for cilia analysis, v.10, Zenodo (2022); https://doi.org/10.5281/zenodo.7417672

51. M. Westerfield, *The Zebrafish Book: A Guide for the Laboratory Use of Zebrafish (Danio Rerio)*. (Univ. of Oregon Press, 2000).

52. M. C. LaFave, G. K. Varshney, M. Vemulapalli, J. C. Mullikin, S. M. Burgess, A defined zebrafish line for high-throughput genetics and genomics: NHGRI-1. *Genetics* **198**, 167–170 (2014). doi:10.1534/genetics.114.166769 Medline

53. Z. Sun, A. Amsterdam, G. J. Pazour, D. G. Cole, M. S. Miller, N. Hopkins, A genetic screen in zebrafish identifies cilia genes as a principal cause of cystic kidney. *Development* **131**, 4085–4093 (2004). doi:10.1242/dev.01240 Medline

54. C. B. Kimmel, W. W. Ballard, S. R. Kimmel, B. Ullmann, T. F. Schilling, Stages of embryonic development of the zebrafish. *Dev. Dyn.* **203**, 253–310 (1995). doi:10.1002/aja.1002030302 Medline

55. E. Schäffer, S. F. Nørrelykke, J. Howard, Surface forces and drag coefficients of microspheres near a plane surface measured with optical tweezers. *Langmuir* **23**, 3654–3665 (2007). doi:10.1021/la0622368 Medline

56. N. A. Duldulao, S. Lee, Z. Sun, Cilia localization is essential for in vivo functions of the Joubert syndrome protein Arl13b/Scorpion. *Development* **136**, 4033–4042 (2009). doi:10.1242/dev.036350 Medline

57. R. M. Power, J. Huisken, A guide to light-sheet fluorescence microscopy for multiscale imaging. *Nat. Methods* **14**, 360–373 (2017). doi:10.1038/nmeth.4224 Medline

58. A. Edelstein, N. Amodaj, K. Hoover, R. Vale, N. Stuurman, Computer control of microscopes using microManager. *Curr. Protoc. Mol. Biol.* mb1420s92 (2010). doi:10.1364/OE.17.017190

59. M. Mahamdeh, E. Schäffer, Optical tweezers with millikelvin precision of temperature-controlled objectives and base-pair resolution. *Opt. Express* **17**, 17190–17199 (2009). doi:10.1364/OE.17.017190 Medline

60. E. Fällman, O. Axner, Design for fully steerable dual-trap optical tweezers. *Appl. Opt.* **36**, 2107–2113 (1997). doi:10.1364/AO.36.002107 Medline

61. M. Mahamdeh, C. P. Campos, E. Schäffer, Under-filling trapping objectives optimizes the use of the available laser power in optical tweezers. *Opt. Express* **19**, 11759–11768 (2011). doi:10.1364/OE.19.011759 Medline

62. F. Hörner, R. Meissner, S. Polali, J. Pfeiffer, T. Betz, C. Denz, E. Raz, Holographic optical tweezers-based in vivo manipulations in zebrafish embryos. *J. Biophotonics* **10**, 1492–1501 (2017). doi:10.1002/jbio.201600226 Medline

63. I. A. Favre-Bulle, A. B. Stilgoe, H. Rubinsztein-Dunlop, E. K. Scott, Optical trapping of otoliths drives vestibular behaviours in larval zebrafish. *Nat. Commun.* **8**, 630 (2017). doi:10.1038/s41467-017-00713-2 Medline

64. P. L. Johansen, F. Fenaroli, L. Evensen, G. Griffiths, G. Koster, Optical micromanipulation of nanoparticles and cells inside living zebrafish. *Nat. Commun.* **7**, 10974 (2016). doi:10.1038/ncomms10974 Medline

65. J. Howard, *Mechanics of Motor Proteins and the Cytoskeleton*. (Sinauer Associates, 2001).

66. A. A. Akerberg, C. E. Burns, C. G. Burns, C. Nguyen, Deep learning enables automated volumetric assessments of cardiac function in zebrafish. *Dis. Model. Mech.* **12**, dmm.040188 (2019). doi:10.1242/dmm.040188 Medline

67. J. Schindelin, I. Arganda-Carreras, E. Frise, V. Kaynig, M. Longair, T. Pietzsch, S. Preibisch, C. Rueden, S. Saalfeld, B. Schmid, J.-Y. Tinevez, D. J. White, V. Hartenstein, K. Eliceiri, P. Tomancak, A. Cardona, Fiji: An open-source platform for biological-image analysis. *Nat. Methods* **9**, 676–682 (2012). doi:10.1038/nmeth.2019 Medline

68. T. W. Chen, T. J. Wardill, Y. Sun, S. R. Pulver, S. L. Renninger, A. Baohan, E. R. Schreiter, R. A. Kerr, M. B. Orger, V. Jayaraman, L. L. Looger, K. Svoboda, D. S. Kim, Ultrasensitive fluorescent proteins for imaging neuronal activity. *Nature* **499**, 295–300 (2013). doi:10.1038/nature12354 Medline

69. N. C. Shaner, M. Z. Lin, M. R. McKeown, P. A. Steinbach, K. L. Hazelwood, M. W. Davidson, R. Y. Tsien, Improving the photostability of bright monomeric orange and red fluorescent proteins. *Nat. Methods* **5**, 545–551 (2008). doi:10.1038/nmeth.1209 Medline

70. R. F. Laine, K. L. Tosheva, N. Gustafsson, R. D. M. Gray, P. Almada, D. Albrecht, G. T. Risa, F. Hurtig, A.-C. Lindås, B. Baum, J. Mercer, C. Leterrier, P. M. Pereira, S. Culley, R. Henriques, NanoJ: A high-performance open-source super-resolution microscopy toolbox. *J. Phys. D Appl. Phys.* **52**, 163001 (2019). doi:10.1088/1361-6463/ab0261 Medline

71. L. Djenoune, R. Tomar, A. Dorison, I. Ghobrial, H. Schenk, J. Hegermann, L. Beverly-Staggs, A. Hidalgo-Gonzalez, M. H. Little, I. A. Drummond, Autonomous Calcium Signaling in Human and Zebrafish Podocytes Controls Kidney Filtration Barrier Morphogenesis. *J. Am. Soc. Nephrol.* **32**, 1697–1712 (2021). doi:10.1681/ASN.2020101525 Medline

72. E. J. G. Peterman, F. Gittes, C. F. Schmidt, Laser-induced heating in optical traps. *Biophys. J.* **84**, 1308–1316 (2003). doi:10.1016/S0006-3495(03)74946-7 Medline

73. S. Ebert, K. Travis, B. Lincoln, J. Guck, Fluorescence ratio thermometry in a microfluidic dual-beam laser trap. *Opt. Express* **15**, 15493–15499 (2007). doi:10.1364/OE.15.015493 Medline